

Chapter 2

Cyber-physical Modeling of Hybrid Vehicles

2.1 Introduction

For model-based control of *hybrid vehicles*, an appropriate model is essential. Here, we explain that “appropriate” needs to be read in the context of the goal of the model. It does not make much sense to derive a model taking all possible physical effects into account, to realize later that the data available to validate the model come from experiments which are not particularly reproducible or do not provide enough or accurate enough information, or that the model does not integrate well with computational processes. We also do not need all possible accuracy for control because feedback is quite robust. Therefore, we need to use, and have the freedom to use, approximate models, which should cover the main characteristics of the physics, allow extensive analysis and be implementable in real-time situations for online control. The last characteristic will shift in time, what is not possible today will be possible in a few years. It allows us to aim for the boundaries of what is technically possible today, knowing it will be easy to achieve in the future. All components of the drivetrain need those models, which means internal combustion engine, electric machine, battery, and their interconnections. We primarily use prescribed or registered drive cycles, so do not consider driving and drivability issues. We focus on system level control, not on component level control. Thus, torque- or current-based models will get limited attention. Power-based models will receive full consideration.

There are several approaches to modeling system components, and the complexity of available models may vary widely. For example, *combustion engine* models may be crank angle resolved, or crank angle averaged, or even quasi-static. The same variety holds for *electric machine* models. Crank angle resolved or averaged models are useful for the design of component controllers, e.g., engine controllers that determine the valve, fuel injection or spark ignition timings, or that select the exhaust gas recirculation or inlet manifold boost pressure. Those models are more complicated than needed and do not allow an extensive analysis of the basic problem. They also model phenomena that are of no interest for the basic problem. This is due to the slow storage dynamics of the storage devices, which normally take on the order of several minutes or hours to be discharged or charged. Some electro-chemical

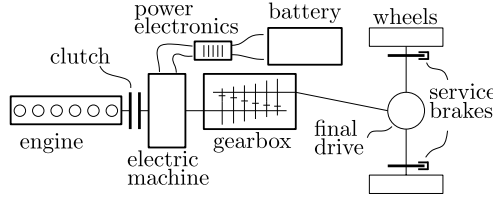


Fig. 2.1 Overview of drivetrain components in a parallel hybrid electric truck. Note the connecting elements clutch, axle, gearbox, final drive, and power electronics besides the power converters (engine and electric machine) and battery

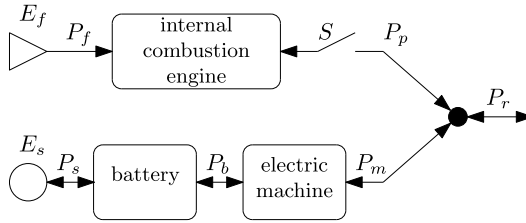


Fig. 2.2 Schematic overview of a hybrid drivetrain including the internal combustion engine (chemical to mechanical power converter), the electric machine (electrical to mechanical power converter), and the battery (electro-chemical to electrical power converter). A switch, S , represents the clutch. Other connecting elements are indicated by arrows representing power transfer over a powernet (e.g., realized with a wiring harness). The *arrows* are one-sided for irreversible processes and two-sided for reversible processes. Energy storage is represented by E_f (fuel tank) and E_s (battery). The *solid circle* represents power compounding. Compared to Fig. 1.5 P_i is omitted

processes in a *battery* may be much faster than that, however, but the dominant time scale is in the order of minutes. It is also due to the slow temporal changes in power flow in the vehicle, based both on data from the drive cycles, which are typically time resolved at 1 [s] intervals, and on real practice, where a human driver will not perpetually change his demands in split seconds because this is not compatible with the normal flow of traffic. This implies that time needs to be resolved in the order of seconds. Because the usual power converters have a cycle time below 0.1 [s], angle resolved or even angle averaged models provide too much detail. We will, therefore, use quasi-static models for the power converters and a low order dynamic model for the storage device. The remainder of this chapter will provide details.

2.2 Hybrid Vehicle Definitions

Figure 2.1 shows an example of a drivetrain layout for a hybrid electric truck. An overview of these components and their interconnections is presented in this section.

Figure 2.2 depicts a schematic overview of a hybrid electric drivetrain. The mechanical output power of the internal combustion engine P_p and electric machine

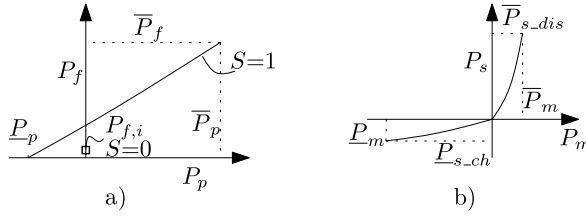


Fig. 2.3 Schematic cost functions of (a) internal combustion (Diesel) engine and (b) electric machine and battery. Note that with the clutch open the engine may run at idle speed, indicated by the \square , but could also be stopped to achieve $P_f = 0$. Furthermore, for $P_p < 0$ the fuel use P_f is interpolated, but for some engines, e.g., Otto engines, this is not possible and the only feasible operating point is then $P_p = \underline{P}_p$ when the fuel flow is cut off

P_m matches the power requested by the driver or cruise controller P_r :

$$P_r = P_p + P_m \quad (2.1)$$

because there is no possibility to store energy in this point. The torque conversion is supposed to be perfect, so power is just added or subtracted, which is most easily achieved if combustion engine and electric machine are put on the same axle.

The conversion of fuel power P_f to the engine output power P_p is modeled as a function of the power throughput:

$$P_f(S, \omega, P_p) = \begin{cases} P_{f,i} & \text{for } S = 0, \\ P_{f,p}(\omega, P_p) & \text{for } S = 1, \end{cases} \quad (2.2)$$

where S is a Boolean variable modeling clutch opening, $P_{f,i} \geq 0$ is the fuel power during idling, $P_{f,p}$ is the fuel power if tractive power is delivered, and ω is the rotational velocity. If $S = 0$ than $P_p = 0$. When stop-start of the engine is possible then $P_{f,i} = 0$ if $S = 0$, see Fig. 2.3a. Section 2.3.1 presents typical relations for P_f .

The fuel power P_f is related to the fuel mass flow rate \dot{m}_f (or fuel rate, for short) by the lower heating value, h

$$P_f = h\dot{m}_f.$$

The characteristics of the hybrid drivetrain components require a non-smooth model in many hybrid vehicle applications, where charging and discharging is modeled with a non-smooth continuous function, see Fig. 2.3b. The combined conversion of storage power P_s to the electric power P_b , and of P_b to the mechanical power P_m is, therefore, modeled as a non-smooth function of the power throughput:

$$P_s(P_m, E_s) = \begin{cases} P_{s_ch}(P_m, E_s) & \text{for } P_m < 0, \\ P_{s_dis}(P_m, E_s) & \text{for } P_m \geq 0, \end{cases} \quad (2.3)$$

with $P_{s_ch}(0, E_s) = P_{s_dis}(0, E_s)$, in which P_{s_ch} is the storage power during charging of the battery and P_{s_dis} the storage power during discharging of the battery,

see Fig. 2.3b. The conversion process (2.3) could depend (smoothly) on the stored energy in the battery E_s . It is assumed that the influence of other variables on the conversion losses, e.g., rotational velocity of the electric machine, temperature, and aging are known, and are incorporated in the power conversion function at time t . Note also that the drag power of the electric machine is always present (since decoupling the electric machine from the wheels is not possible in the topology considered) and is incorporated in the power request P_r such that $P_m = 0$ if $P_s = 0$. Typical relations for P_m and P_b are in Sect. 2.3.2 while those for P_b and P_s are in Sect. 2.3.3.

2.3 Models of Hybrid Powertrain Components

Mathematical models will be presented, together with a physical interpretation of models and model assumptions. Those models will describe the system dynamics in a rudimentary form. They will represent, in an approximate way, the power losses incurred by the power converters, and they will stress the physical, technical, and economic limitations on power flows and energy levels.

2.3.1 Combustion Engine

The derived models try to give a sufficiently accurate relation between the mechanical power delivered by an engine and the chemical power (fuel power) needed. Several models are possible that try to represent experimental data but also try to have a (very) simple representation. Different trade-offs are possible, resulting in models of different complexities.

It is beneficial to analyze some experimental results, and extract characteristic properties from these results, before presenting the models.

An example of the fuel use for a naturally aspirated spark-ignition (Otto) engine for a mid-sized passenger car is given in Fig. 2.4. Another example is for a compression-ignition (Diesel) engine used in a delivery truck in Fig. 2.5.

Note that both these figures represent the same type of data, but the data are presented in a totally different way, enabling a different view on the data. A representation like Fig. 2.4 of the data in Fig. 2.5 is given in Fig. 2.6.

The main contributing factors to fuel use are

1. the delivered mechanical power, $P_p = \omega T_p$, as can be seen from the slope of the fuel use curve as a function of power, see Figs. 2.4 and 2.6,
2. the rotational speed, ω , which influences the drag losses as can be seen from the drag torque curve, where $P_f = 0$, in Fig. 2.5.

There are many more factors influencing fuel use, such as air properties like temperature, pressure, and humidity, fuel properties like fuel composition (blend), octane

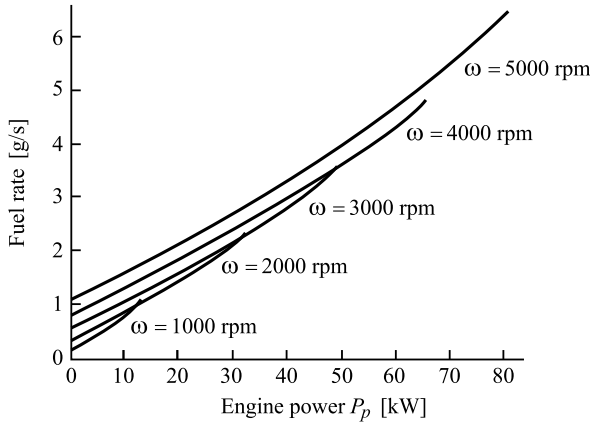


Fig. 2.4 Interpolated line plot of spark-ignition engine fuel rate as a function of mechanical power P_p at the crankshaft and of crankshaft rotational velocity ω under steady-state conditions, for a set of different velocities. Note that these data, especially near maximum torque requests, need to be approximated by at least a quadratic relation. The fuel rate increase near maximum torque is typically related to an enriched fuel mixture commanded by the engine controller and meant to cool the valves

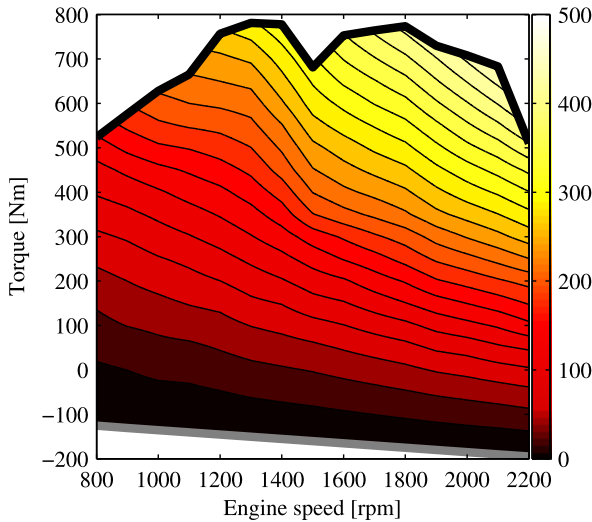


Fig. 2.5 Interpolated and quantized contour plot of measured diesel engine fuel power consumption P_f as a function of reconstructed crankshaft torque T_p and measured crankshaft rotational velocity ω_p under steady-state conditions, for a set of different velocities and gas pedal positions. The *dark line* indicates the maximum engine torque, \bar{T}_p , and the *gray line* indicates the engine drag torque, \underline{T}_p , while different color shades represent different fuel consumption levels as indicated by the right-hand scale in [kW]. The most efficient operating points are those with a hyperbola (constant mechanical power level) as tangent. The dip in maximum torque at $\omega_p \approx 1500$ [rpm] is due to emission restriction measures in the engine controller

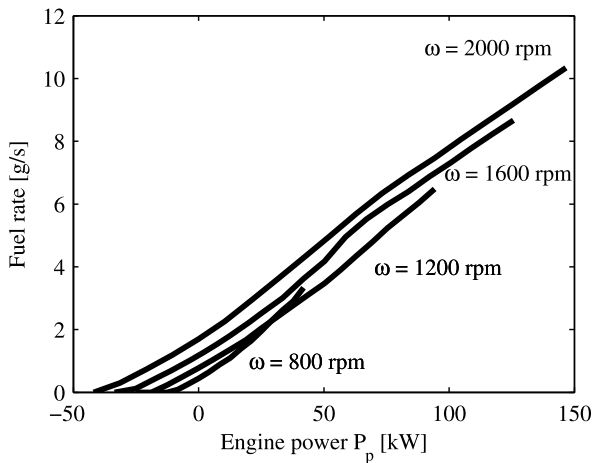


Fig. 2.6 Interpolated line plot of compression-ignition engine fuel rate as a function of mechanical power P_p at the crankshaft and of crankshaft rotational velocity ω under steady-state conditions, for a set of different velocities. Note that a *straight line*, with off-set depending on velocity ω , could be used to approximate these data, but essentially the data do not quite lie on a straight line, in particular at low speeds, and do not even represent a convex relation. On the other hand, some variability in the data is created by the engine controller trying to meet emission standards in certain critical operating points defined in the test procedure, but for a hybrid drivetrain with a lower fuel throughput, so lower emissions, another calibration without this variability can be permitted

number, and volatility, engine properties like age, wear, and maintenance state, etc., but in particular measures built into the engine controller that aim at reducing emissions. It is assumed that most of these effects are averaged out, are sufficiently small to be neglected, or can be included via model parameters.

The main differences between fuel rate results for Otto and Diesel engines or between light and heavy-duty engines are that

1. the fuel rate as a function of delivered power appears to be straighter for a Diesel engine than for an Otto engine, so for a Diesel engine an affine relation may be appropriate, whereas for an Otto engine a strictly convex relation may be better, although more careful analysis shows that this depends for a large part on the engine controller calibration, so that is the distinguishing feature,
2. drag losses are higher for heavy-duty engines than for light-duty engines, leading to higher overall losses for heavy-duty engines compared to light-duty engines for the same power fraction, compare Figs. 2.4 and 2.6, but the dependency on rotational speed looks similar and could be represented by a convex relation,
3. for Otto engines, at part load, throttling losses occur, contrary to Diesel engines, leading to higher intermediate power losses for Otto engines compared to Diesel engines from the same duty category, yielding a higher slope in an affine relation,
4. Diesel engines profit from a higher compression ratio and thus higher combustion temperatures, yielding a shallower slope in an affine relation.

It appears that static engine models do not need to distinguish between Otto and Diesel engines or between light and heavy-duty engines, the same relations with different numerical values could do. For engine models, one could distinguish between calibrations used in the engine controller, and, based on that, choose a different model structure. We therefore present several models that differ in the description of the influence of power output and fuel use to accommodate this. All models separate the influence of P_p and ω , i.e., the approximating functions are separable.

2.3.1.1 Willans Line (Affine) Model

The fuel consumption of an engine, e.g., the Diesel engine presented in the previous section, at rotational velocity ω , can be approximated with a piecewise affine relation, sometimes referred to as a Willans line approximation (Guzzella and Sciarretta 2005, p. 44):

$$\frac{P_f(\omega, P_p)}{\bar{P}_p} = \max\left(0, \gamma_{p,0}(\omega) + \gamma_{p,1} \frac{P_p}{\bar{P}_p}\right), \quad (2.4)$$

where $P_f \geq 0$ is the fuel power, $\gamma_{p,0}(\omega) > 0$ describes the velocity dependent engine drag loss, ω represents the rotational velocity of the drivetrain, \bar{P}_p denotes the maximum power output of the engine, and $\gamma_{p,1} > 1$ is a fuel conversion parameter, see Table 2.1, p. 29, for the values. For component sizing problems, it is convenient to incorporate the maximum power output of the power converters in the cost functions. This also make comparisons between engines, using normalized functions and parameters, easier. At zero fuel consumption, $P_f = 0$, the engine drag power \underline{P}_p is:

$$\frac{\underline{P}_p(\omega)}{\bar{P}_p} = \frac{-\gamma_{p,0}(\omega)}{\gamma_{p,1}} < 0. \quad (2.5)$$

The power of a combustion engine, or any other primary power converter, is limited, where the limit depends on the rotational velocity:

$$\underline{P}_p(\omega) \leq P_p \leq \bar{P}_p(\omega), \quad (2.6)$$

where the admissible range for P_p may be further restricted due to relation (2.1).

2.3.1.2 Strictly Convex Polynomial Equation Model

The fuel use of an engine, e.g., the Otto engine presented in the previous section, at rotational velocity ω , can be described by a strictly convex function, for which we choose a quadratic one with no provision for scaling as we will not use this model for component sizing problems

$$P_f(\omega, P_p) = \max(0, \gamma_{p,0}(\omega) + \gamma_{p,1} P_p + \gamma_{p,2} P_p^2), \quad (2.7)$$

with $\gamma_{p,1} > 1$ the linear fuel conversion parameter, and $\gamma_{p,2} > 0$ the quadratic fuel conversion parameter. These will be fitted in such a way that an accurate local approximation is achieved towards the measured fuel rate data. The interval of fitted data will be determined by the nominal value of P_p and the range in power achievable by manipulating the electric machine mechanical power, P_m , while still meeting the traction power requested, P_r . Note that this model is only valid in a restricted interval for P_p , because if $P_p \ll 0$ it gives $P_f > 0$, which will not occur in practice. Relations similar to (2.6) also hold.

2.3.2 Electric Machine

Different electric machines are used in HEVs. They may range from up-scaled alternators to powerful direct drive solutions. Here, we present a model for a powerful 44 [kW] motor/generator, but other electric machines could use the same model, albeit with different numerical values.

The motor/generator model, including the power electronics (inverter) used to get the correct DC conditions for the battery, is based on experimental data obtained in equilibrium points. The model aims to present the power losses accurately, but does not aim to represent transient behavior. The power losses could be represented by a (multi-dimensional) table, but are here fitted with simple analytical expressions to allow for deeper analysis.

The conversion of electric machine mechanical power, P_m , to electrical power, P_b , and vice versa, is measured under steady-state conditions, see Fig. 2.7. An analysis of the data shows that a non-smoothness is present and that the relation is not necessarily convex. To indicate this, the gradient $\partial P_b / \partial P_m$, at one rotational velocity, is depicted in Fig. 2.8.

The conversion characteristics of the electric machine are approximated with two piecewise quadratic functions with a non-smooth convex union:

$$\frac{P_b(\omega, P_m)}{\bar{P}_m} = \begin{cases} \gamma_{m,0}(\omega) + \gamma_{m,1}^+ \frac{P_m}{\bar{P}_m} + \gamma_{m,2}^+ \left(\frac{P_m}{\bar{P}_m}\right)^2, & \text{for } P_m \geq 0 \text{ (motoring)} \\ \gamma_{m,0}(\omega) + \gamma_{m,1}^- \frac{P_m}{\bar{P}_m} + \gamma_{m,2}^- \left(\frac{P_m}{\bar{P}_m}\right)^2, & \text{for } P_m < 0 \text{ (generating)} \end{cases} \quad (2.8)$$

with the electric power P_b , electric machine drag function $\gamma_{m,0}(\omega) > 0$, parameters $\gamma_{m,1}^+ > 1$, $\gamma_{m,2}^+ > 0$, $\gamma_{m,1}^- < 1$, $\gamma_{m,2}^- > 0$, and the maximum motoring power of the electric machine \bar{P}_m to allow for easy scaling of the size of the electric machine.

When the vehicle velocity and gearshift trajectory are prescribed, the rotational velocity ω , and parameters $\gamma_{p,0}$ and $\gamma_{m,0}$, are also known. It is assumed that the electric machine is always connected to the vehicle wheels such that the drag power of the electric machine $\gamma_{m,0}$ is present anyway, and can, therefore, be incorporated in the power request P_r . Furthermore, it is assumed that the relation $P_m \rightarrow P_b$ is monotonically increasing in the domain of interest, i.e., $\partial P_b / \partial P_m \geq 0$, see Fig. 2.8.

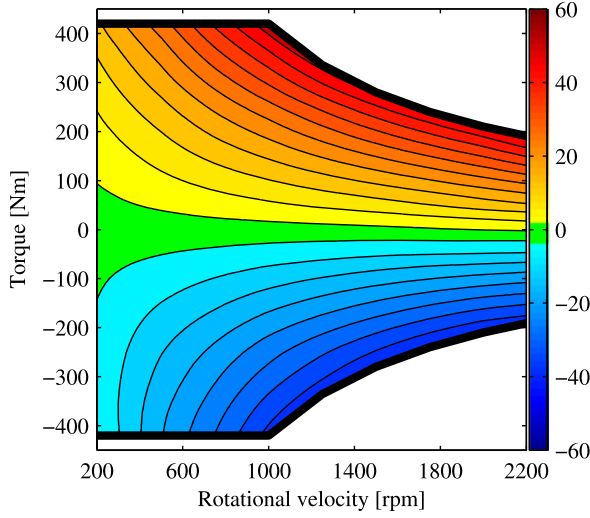


Fig. 2.7 Interpolated and quantized contour plot of electric power P_b as a function of electric machine torque T_m and rotational velocity ω_m . The *upper dark line* indicates the maximum electric machine torque \bar{T}_m , the *lower dark line* indicates the maximum generator torque \underline{T}_m , while *different color shades* represent different electric power levels as indicated by the right-hand scale in kW. The operating points with the smallest losses on a contour line are those with a hyperbola (constant mechanical power level) as tangent

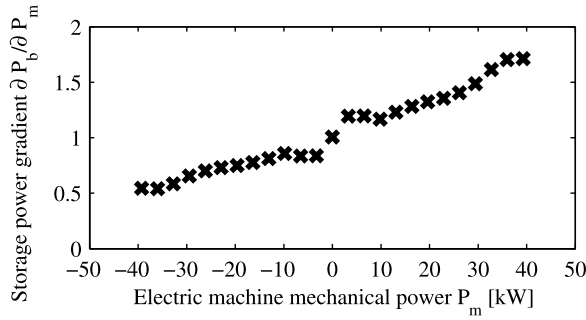


Fig. 2.8 Electric power gradient $\partial P_b / \partial P_m$ as a function of electric machine mechanical power P_m for rotational velocity $\omega = 1000$ [rpm]. The gradient is discontinuous, so the function $P_b(\omega, P_m)$ is non-smooth. Furthermore, since this gradient is evidently not a monotonic increasing relation, the functions $P_b(\omega, P_m)$, one for each interval of P_m , are not necessarily convex in P_m , but could be approximated as convex ones without large errors

Just as for the combustion engine, the electric machine power is limited

$$\underline{P}_m(\omega) \leq P_m \leq \bar{P}_m(\omega). \quad (2.9)$$

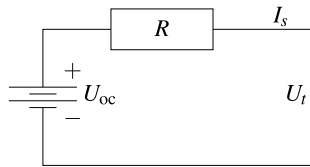


Fig. 2.9 Equivalent circuit for a battery. The open-circuit voltage U_{oc} will be a function of the state-of-energy E_s , but in principle not of P_s , while the terminal voltage U_t will be a function of P_s . The resistance R may be a function of temperature and of state-of-energy, or even of charging history, and may also attain values that differ for charging and discharging

The admissible range for the electric machine power may even be smaller, due to relation (2.1) and the limited power range for the primary power converter (2.6).

2.3.3 Storage Device

The main dynamics of an HEV storage device is rather slow compared to other components in the drivetrain, i.e., the characteristic time in which this device is charged or discharged is quite long. Therefore at least the storage dynamics needs to be accounted for, which can be done by a conservation law

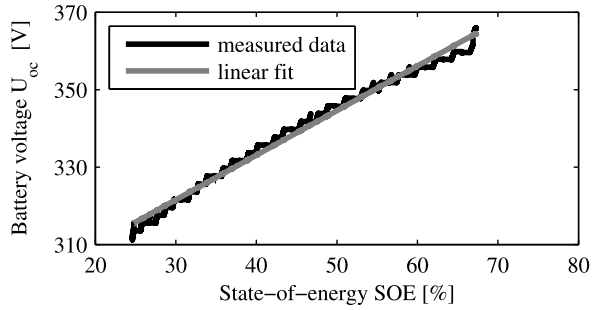
$$E_s(t) = E_s(t_0) + \int_{t_0}^t -P_s(\tau) d\tau, \quad (2.10)$$

where E_s is the energy stored in the battery and P_s is the power flow. The minus-sign is due to the convention that P_s is positive for power flowing out of the battery.

Apart from the conservation law, we need some constitutive relations from which the losses of the processes involved follow. These relations for storage devices—here we only consider electro-chemical storage—may differ depending on the electro-chemistry used. We consider two types, a battery model with *Ohmic losses*, based on an equivalent circuit, and a simplified model that could be found by fitting experimental data, but could also be found assuming a constant open-circuit voltage (or constant electro-motive force in electro-chemistry parlance), independent of the charge level. The constant open-circuit voltage assumption may be valid for Li-ion batteries with a flat characteristic or for lead-acid batteries in a restricted range of charge levels, but it will not be valid for, e.g., super capacitors in their full range.

To propose a reasonable model, first some experimental results are presented. They describe the battery voltage as a function of charge state. From that, the battery internal resistance can be reconstructed. The idea is to model the battery based on a circuit with a voltage source (battery open-circuit voltage) and a resistance, while only the battery terminal voltage and current are measurable, see Fig. 2.9. The power losses can then be computed from the current and the Ohmic loss due to the resistance, see Pop et al. (2008).

Fig. 2.10 Measured and quantized battery open-circuit voltage U_{oc} as a function of the state-of-energy SOE averaged over a slow charging/discharging cycle. This is a monotonic increasing relation, almost a straight line as indicated by the approximation: an affine relation



2.3.3.1 “Equivalent Circuit”-Based Battery Model

For a certain HEV storage system with Li-ion batteries, the open-circuit voltage U_{oc} is estimated by discharging the battery with the lowest possible current request (where the vehicle drives at a foot pace), see Fig. 2.10. Under the assumption that the internal resistance R is equal for charging and discharging (Pop et al. 2008), the measured terminal voltage U_t during charging and discharging is averaged to estimate U_{oc} . The measured voltage is quantized with a 2 [V] quantization interval. Given these data, obtained at an almost constant temperature, there is no way we can model the influence of temperature on the (dis)charging process, so this influence is neglected. In practice, the battery pack temperature is tightly controlled to avoid chemical process instabilities and is kept low to reduce battery wear, so this assumption seems reasonable.

Figure 2.10 shows that a fully charged battery has a higher voltage than a depleted battery. Therefore, a charged battery requires a lower current to deliver a certain power request, and the internal losses are then also smaller.

Given the estimated open-circuit voltage U_{oc} , the measured terminal voltage U_t and current I_s , the battery internal resistance is estimated with

$$R = \frac{U_{oc} - U_t}{I_s} = \frac{U_R}{I_s}, \quad (2.11)$$

where U_R is the voltage drop over the resistor. Here, charging and discharging are treated as equal. The computed internal resistance for one charge/discharge cycle is depicted in Fig. 2.11.

The battery open-circuit voltage U_{oc} is approximated with an affine function of the state-of-energy:

$$U_{oc}(E_s) = U_0 + \phi E_s, \quad (2.12)$$

where U_0 is the voltage of a fully discharged battery, $\phi \geq 0$ is the battery open-circuit voltage increase factor, and E_s is the energy stored in the storage device. This approximation is depicted in Fig. 2.10 and shows satisfactory agreement with the experimental data.

When E_s is expressed in a fraction (or %) of the fully charged E_s , i.e., the battery capacity E_c , it is denoted with SOE. The relation with the often used state-of-charge

Fig. 2.11 Reconstructed battery resistance R as a function of the state-of-energy SOE for slowly charging and discharging. Both graphs are concave, are almost at the same level, and could be considered equal and constant given the wide spread in the data

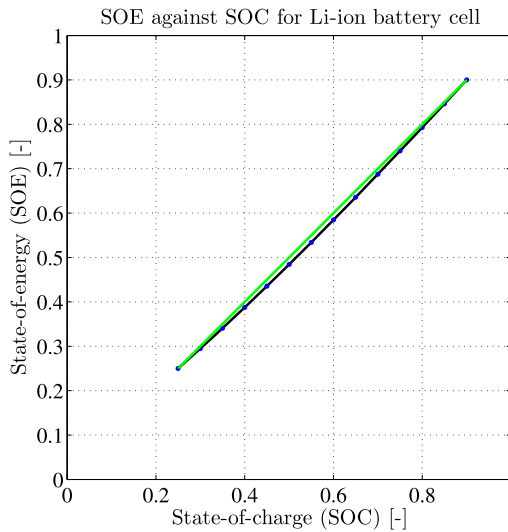
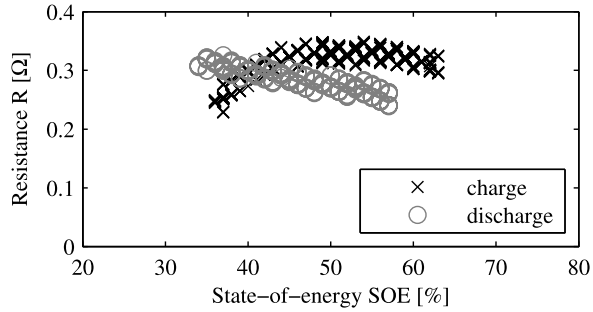


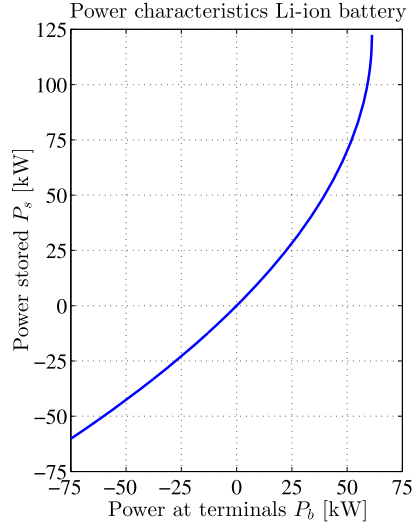
Fig. 2.12 State-of-energy versus state-of-charge for a single Li-ion cell. The figure uses experimental data directly (indicated with *circles*). Note that this graph can be shifted up or down, depending on the initial condition used when solving differential equation (2.13) for E_s , and it can be stretched, depending on the assumed energy capacity E_c . Here, it is re-normalized to match the diagonal (green) exactly in 2 points, so SOE and SOC are both equal at the values 0.25 and 0.90, marking the interval for which data are used. The diagonal (green) is obtained if a fixed value for U_{oc} , so ϕE_s is constant in (2.13), is used to compute E_s from I_s

$Q_s(t) = Q_s(t_0) + \int_{t_0}^t -I_s(\tau) d\tau$, or SOC when expressed as a fraction of the total charge capacity of the battery, is via (2.12) and $P_s = I_s U_{oc}$, so

$$\dot{E}_s = -I_s(U_0 + \phi E_s). \quad (2.13)$$

An example for the relation between Q_s , or SOC, and E_s , or SOE, is in Fig. 2.12.

Fig. 2.13 Computed battery power at the terminals versus battery power stored for a Li-ion battery with the lowest possible $U_{oc} = 280$ [V], representing the worst case with the highest losses. Note that for $P_b > 61.25$ [kW], corresponding to 122.5 [kW] for P_s , no solution is possible, i.e., no more than that amount of power can be extracted from the battery given the assumed electrical model for the battery, which becomes dubious for these power levels where U_t approaches $U_{oc}/2$



It is suggested to approximate the battery loss power with an internal resistance model, Pop et al. (2008):

$$P_s(\omega, P_m, E_s) = I_s U_{oc}(E_s) = R I_s^2 + P_b(\omega, P_m), \quad (2.14)$$

or, as polynomial in I_s ,

$$R I_s^2 - U_{oc} I_s + P_b(\omega, P_m) = 0, \quad (2.15)$$

where R is the internal resistance which, for simplicity, may be assumed to be constant. Current I_s is solved from the quadratic relation (2.15):

$$I_s = \frac{U_{oc}(E_s) - \sqrt{U_{oc}^2(E_s) - 4R P_b(\omega, P_m)}}{2R}, \quad (2.16)$$

where P_m is limited from above such that $U_{oc}^2 \geq 4R P_b(\omega, P_m)$ or $U_t \geq U_{oc}/2$. This bound is the maximum amount of power that can be extracted from the battery and corresponds to the case where the internal resistance R equals the resistance over the terminals, when $U_t = U_{oc}/2$. If P_m is too large, i.e., $P_b > \frac{U_{oc}^2}{4R}$, there is no (real) solution for (2.14). Relation (2.14) is represented in graphical form in Fig. 2.13. The model for a lead acid battery can be developed in the same way.

To protect the battery from under- or overcharging, the battery energy levels are constrained:

$$E_s(t) - \overline{E}_s \leq 0, \quad (2.17)$$

$$\underline{E}_s - E_s(t) \leq 0, \quad (2.18)$$

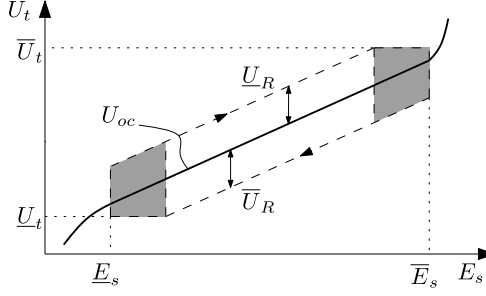


Fig. 2.14 Mixed constraints on battery state-of-energy and voltage. Variables \underline{U}_R and \overline{U}_R are the voltage drops over the resistor due to the maximal and minimal power at the terminals. The voltage bounds on U_t lead to combined input (power) and state (SOE) constraints in the neighborhood of $(\underline{E}_s, \underline{U}_t)$ and $(\overline{E}_s, \overline{U}_t)$

here, $\overline{E}_s < E_c$ is the maximum allowable state-of-energy of the storage device which is lower than the maximum capacity $\underline{E}_s > 0$ is the minimum one. The allowable range for E_s lies strictly inside the physical possible range for E_s , aiming to reduce wear of the battery, which is largest near the boundaries of the physical range. Equations (2.17) and (2.18) are “pure” state constraints meaning that they are a function of the state only. Any of the variables P_s , P_b , or P_m can be used as independent variable such that the state constraints (2.17) and (2.18) are of first order, meaning that the first time derivative of the constraints (2.17) and (2.18) contains the control explicitly. It may also be necessary to use a combination of P_s and E_s to express constraints on the voltage level, so-called mixed state/input constraints. Those mixed constraints are more difficult to handle than isolated input and state constraints. See Fig. 2.14 for an example.

2.3.3.2 “Fitted” Battery Model

One of the most straightforward ways to develop a simplified battery model is to assume a certain loss for charging, proportional to charging power squared. Because the current corresponding to a certain power will depend on voltage, we also need to access voltage. However, Li-ion batteries as well as, but to a lesser degree, lead-acid batteries have a relatively weak relation between charge state and voltage. It may, therefore, suffice to neglect this relation if the parameters of the relation are fitted on a restricted interval of operating conditions.

Looking at battery model (2.14), we can also write this as

$$P_s = P_b + \beta_2 P_s^2, \quad (2.19)$$

with $\beta_2 = R/U_{oc}^2 > 0$, where β_2 may depend on R and U_{oc} or may be considered as a constant fitted to measured data corresponding to the interval of interest for the

Fig. 2.15 Battery power stored versus battery power at the terminals for two different approximating functions, (2.19) (red and solid) and (2.21) (green and dashed). Note that both approximations will only agree in a restricted interval around $P_b = 0$, but given the size of the electric machine (the 44 [kW] one) this is precisely the interval of interest

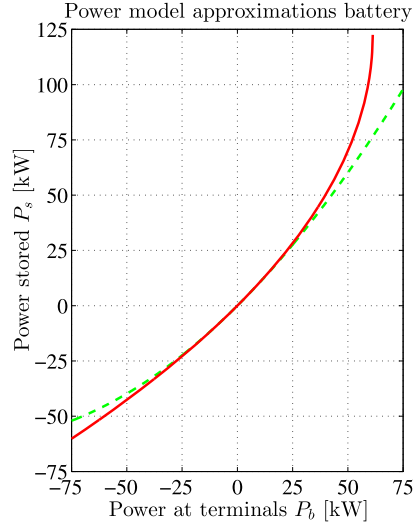


Table 2.1 Hybrid electric delivery truck model parameters; the electric machine drag power is set to 0, but it may be assumed that the power request P_r absorbs this power

Name	Description	Value	Unit
\bar{E}_s	Upper capacity bound	4.08	MJ
\underline{E}_s	Lower capacity bound	1.80	MJ
$\max_{\omega} \bar{P}_p$	Maximum combustion engine power	127.7	kW
$\max_{\omega} \bar{P}_m$	Maximum electric machine power	44.1	kW
R	Battery internal resistance	0.32	Ω
U_0	Discharged battery voltage	280	V
ϕ	Voltage increase factor	21	V/MJ
$\gamma_{m,0}$	Drag electric machine	0	kW
$\gamma_{m,1}^+$	Electric to mechanical cost	1.1200	–
$\gamma_{m,2}^+$	Electric to mechanical cost	0.1323	–
$\gamma_{m,1}^-$	Mechanical to electric cost	0.8800	–
$\gamma_{m,2}^-$	Mechanical to electric cost	0.2205	–
$\gamma_{p,0}$	Engine drag	0.1181	–
$\gamma_{p,1}$	Incremental fuel cost	3.20	–

retrieved or stored power P_s . Solving for P_s gives

$$P_s = \frac{1 - \sqrt{1 - 4\beta_2 P_b}}{2\beta_2}, \quad (2.20)$$

with again the bound $P_b \leq 1/4\beta_2$ corresponding to $P_s \leq 1/2\beta_2$ for a real solution.

The influence of temperature and state-of-energy of the battery on U_{oc} and R , and of possible differences in R between charging and discharging, are all combined

in the parameter β_2 . This parameter could attain different values depending on the specific conditions for the battery. Those effects could be accounted for in the data used to make a parameter fit for β_2 .

Relation (2.19) perfectly matches the graph in Fig. 2.13 for the nominal value of β_2 because it is exactly the same relation as (2.14). The only advantages of the “equivalent circuit” based model (2.14) compared to the “fitted” model (2.19) are that the former provides a physical interpretation for β_2 , or changes in β_2 , while the latter does not, and that there is no interpretation possible of P_s in terms of current and voltage for the latter model.

It is sometimes convenient to write the losses in terms of P_b , so

$$P_s = \beta_1 P_b + \beta_2 P_b^2, \quad (2.21)$$

with $\beta_1 \approx 1$. This is a different approximating function, which will require a different value for β_1 and β_2 to generate an acceptable fit. The relation also does not provide an upper bound for P_b , any value will do.

In a well designed HEV, the interval of P_b of interest normally allows one to use any of the relations (2.14), (2.19), or (2.21), because they are close to each other. Also, the bound on P_b from (2.14) or (2.19) will never be attained, being outside the range that can be covered with the electric machine, see the example in Fig. 2.15.

2.4 Drive Cycles

To validate if engines or complete vehicles meet emission standards several *test procedures* with associated *drive cycles*¹ are available. These cycles are also relevant to address the benefits of hybrid vehicles because they allow to assess CO₂-emissions and fuel economy. The cycles differ with respect to the vehicle type (light or heavy-duty), the main usage of the vehicle (urban, extra-urban, and highway), the regional homologation bodies (Europe, Japan, USA, and others), and distinguish between dynamic (transient) and static (individual operating points), and roller dynamometer (vehicle) and engine dynamometer (engine only) tests.

For passenger or light-duty vehicles the NEDC (New European Driving Cycle) (EEC 1970, pp. 67–73),² see Fig. 2.16, the JC 08 (the new Japanese Cycle), see

¹Most cycles are available in digital form at <http://www.epa.gov/nvfel/testing/dynamometer.htm>.

²The velocity profile during acceleration and deceleration phases for the NEDC is not explicitly given in directive 70/220/EEC (EEC 1970) but is the result of specified acceleration levels and declutch events. Note that there are data sources which do provide a velocity profile, but at least one prominent source does provide a slightly incorrect profile for the urban (ECE) subcycle. In any case, the official specification of the operating cycle contains a handful of obvious errors. Directive 70/220/EEC has been repealed with effect from January 2, 2013 and was replaced by Regulation 83 of the UN/ECE body (UN/ECE 2012). This regulation contains a copy of the same NEDC cycle as in 70/220/EEC, including most of the errors.

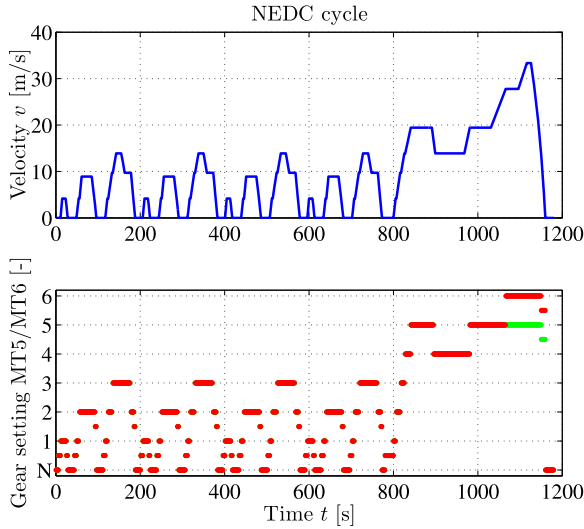


Fig. 2.16 New European Driving Cycle (NEDC) showing velocity and two profiles for manual transmissions with a different number of gears plotted on top of each other. The “N” gear setting means the gearbox is in neutral and the clutch is engaged, the half gear settings indicate that the next higher gear is engaged but the clutch is disengaged. The 11.028 [km] long cycle consists of a four times repeated urban (ECE) subcycle with low velocities taking 195 [s] each and a single extra-urban (EUDC) subcycle with higher velocities starting from $t = 780$ [s] and taking 400 [s] for a complete cycle length of 1180 [s]. The maximum speed is 120 [km/h], the average speed is 33.6 [km/h] including stops and 44.8 [km/h] excluding stops. There is a margin defined around the nominal velocity profile of ± 2 [km/h] and ± 1 [s] which can be exploited to get an up to ≈ 2 % better fuel economy. The declared value for CO_2 emissions may be understated by up to 4 % compared to the measured value (EEC 1980, p. 9). The test cycle is supposed to be started with a cold engine. Because fuel maps of engines are measured at equilibrium conditions, a computation with fuel maps will not exactly reproduce the measured NEDC fuel usage but will give a lower number

Fig. 2.17, and the FTP 75 (Federal Test Procedure) city cycle (CFR40-20 2012b, Appendix I(a) to part 86, pp. 543–546),³ see Fig. 2.18, are relevant.

For future work, the WLTC (World-wide Light-duty Test Cycle) drive cycle may be relevant. This cycle is currently developed for future use (from 2017 on or later) and should simplify homologation (type-approval) by using a single test procedure and test cycle that is valid world-wide. Already several variants are proposed for the test cycle “to accommodate regional differences”, that differ mainly in the maximum speed and acceleration levels.

³The cycle specified here is the so-called UDDS (EPA Urban Dynamometer Driving Schedule for Light-Duty Vehicles and Light-Duty Trucks). The FTP schedule is specified in (FR40-19 2012a, 86.135-12) and is composed of the first 1369 [s] of the 1372 [s] long UDDS, followed by the first 505 [s] of the UDDS to get a hot start phase.

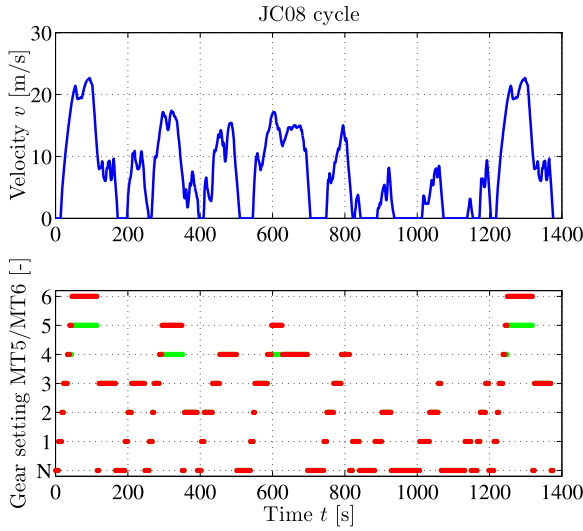


Fig. 2.17 Japanese Cycle (JC 08) showing velocity and two profiles for manual transmissions with a different number of gears plotted on top of each other. The “N” gear setting means the gearbox is in neutral and the clutch is engaged. The cycle represents congested urban traffic. The measurements start after $t = 172$ [s], the part up to $t = 172$ [s] is repeated at the end, while the 8.16 [km] long measurement cycle takes 1204 [s] to complete. The maximum speed is 81.6 [km/h], the average speed is 24.4 [km/h] including stops and 34.7 [km/h] excluding stops. The cycle is performed twice, once with a cold and once with a hot engine

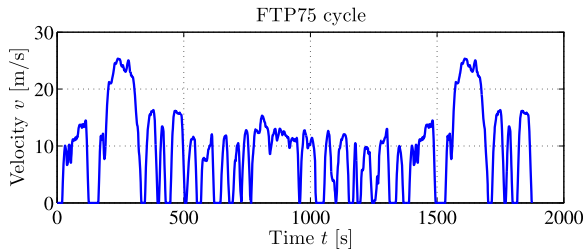


Fig. 2.18 Federal Test Procedure (FTP 75) velocity points. The 17.77 [km] long FTP 75 cycle consists of three phases, where the first and the last one, taking 505 [s], are identical while the middle one takes 864 [s] for a total cycle length of 1874 [s]. The maximum speed is 91.2 [km/h], the average speed is 34.1 [km/h] including stops and 42.2 [km/h] excluding stops. There is a margin defined around the nominal velocity profile of ± 2 [mi/h] and ± 1 [s] (CFR40-20 2012b, p. 546), but the practice of smoothing the speed variations is discouraged. The cycle is started with a cold engine

For heavy-duty vehicles several drive cycles are relevant, e.g., the HD-UDDS (Heavy-Duty Urban Dynamometer Driving Schedule) (CFR40-20 2012b, Appendix I(d) to part 86, pp. 566–573), see Fig. 2.19. Because the characteristics of driving patterns depend on usage, there is a difference between cycles targeted at urban

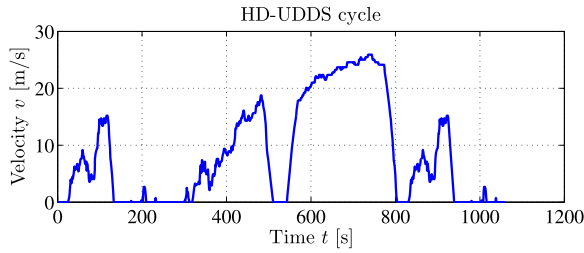


Fig. 2.19 Heavy-duty Urban Dynamometer Driving Schedule (HD-UDDS) speed points. The 8.9 [km] long cycle has two subcycles, one at the beginning and one at the end, that are identical, and that are combined with another subcycle for a total cycle duration of 1060 [s]. The maximum speed is 93.3 [km/h], the average speed is 30.3 [km/h] including stops and 45.4 [km/h] excluding stops, so stops are manifest in the HD-UDDS cycle, approximately one third of the time the vehicle is standing still and the engine is idling

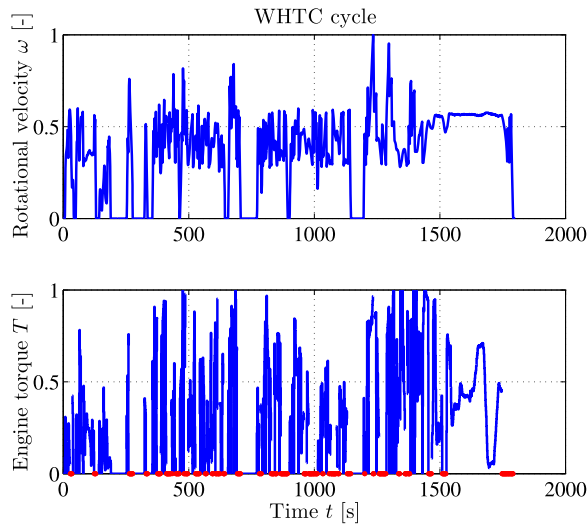


Fig. 2.20 World Harmonised Transient Cycle (WHTC) engine test cycle. Speed and torque are given as a fraction of the working range with the *red torque points* representing closed rack motoring. There are three phases, an urban phase of 900 [s], an extra urban phase of 480 [s], and a highway phase of 420 [s], so the total cycle takes 1800 [s] to complete. The average torque fraction is 0.307 and the average power fraction is 0.201, excluding the closed rack motoring points and assuming idle speed to be 1/3 of maximum speed. This cycle is intended to reduce the homologation effort by engine manufacturers

usage and highway usage for heavy-duty trucks. The vehicle and engine used to perform the cycle need to be characteristic for the class of usage considered.

Some *engine cycles* are available that test only the engine on an engine dynamometer, not the complete vehicle on a roller dynamometer. Engine test cycles are, e.g., the World Harmonised Transient Cycle (WHTC) (UN/ECE 2010,

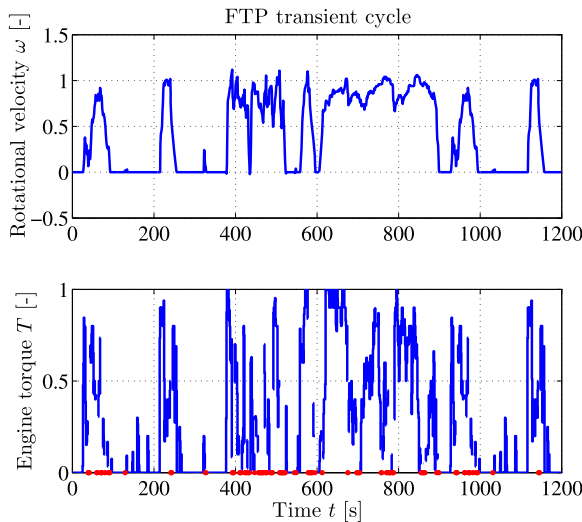


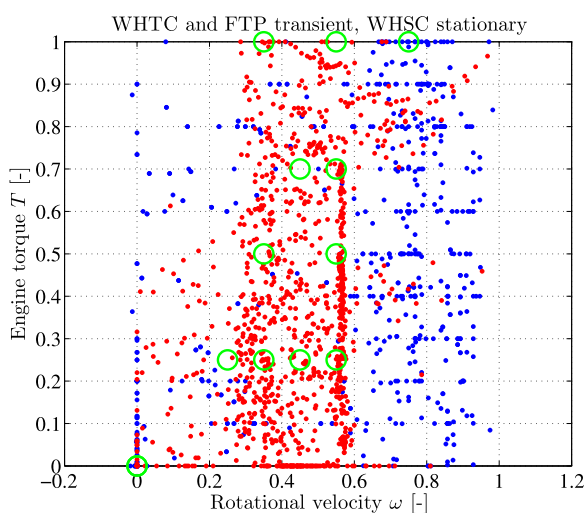
Fig. 2.21 FTP (Federal Test Procedure) Heavy Duty Diesel Transient Cycle (HDDTC). Normalized speed and torque are given as a fraction of the working range, the *red torque points* represent closed rack motoring, the engine torque corresponding to this condition depends on the engine drag torque. Note that speed overrun (speed higher than rated speed, here a fraction > 1) and speed underrun (speed lower than curb idle speed, here a fraction < 0) are specified in the cycle and need to be unnormalized, see (CFR40-20 2012b, Part 86.1333). The cycle consists of four subcycles, where the first is identical to the last, the cycle takes 1199 [s] to complete and is performed twice, once with a cold and once with a hot engine. The average torque fraction is 0.283 and the average power fraction is 0.229, excluding the closed rack motoring points and assuming idle speed to be 1/3 of rated speed

pp. L229/78–L229/89), sometimes called the World Heavy-duty Transient Cycle, and the FTP diesel transient cycle (CFR40-20 2012b, Appendix I(f)(2) to part 86, pp. 585–593). These cycles are depicted in Figs. 2.20–2.21. There are also stationary engine cycles, where the engine is run on a set of specific operating points. An example is the World Harmonised Stationary Cycle (WHSC) (UN/ECE 2010, p. L229/22).

Driving cycles are mostly characterized by a prescribed velocity and gear setting profile as a function of time. This is useful for driving the cycles. For simulations without a driver model, power at the wheel, or engine torque and speed are needed. From velocity and gear profiles it is possible to derive the desired torque and engine speed profile when the total gear ratios, mass, and air and tire resistance characteristics are known, see Eq. (1.1). The resistance characteristics, or road load data, are mostly obtained from preliminary roll-out tests also defined in the test procedures, but for this, a specific vehicle type needs to be defined.

For engine cycles the engine torque and speed, so also engine power, are prescribed as a function of time as can be seen from Figs. 2.20–2.21. For these cycles, torque and speed are scaled towards the performance envelope of the engine under

Fig. 2.22 Comparison of the WHTC (red points), WHSC (green circles), and the FTP transient (blue points, speed overrun corrected to match normalized speed—maximum instead of rated—of other cycles) engine cycles. The data illustrate rather marked differences between those cycles, which will be reflected in fuel economy potential for hybrid systems and their control laws



test. Cycles may be rather different as can be seen from a comparison of the WHTC, WHSC, and FTP transient engine cycles in Fig. 2.22.

2.5 Bibliographical Notes

Several books are available on the subject of (hybrid) vehicles and some effort has been made to introduce or develop (component) models, namely Miller (2004), Guzzella and Sciarretta (2005), Ehsani et al. (2010), Pistoia (2010), Husain (2011), German (2011).

One of the earlier papers on the modeling of hybrid vehicles stems from 1995 Bailey and Powell (1995). An overview of modeling methods is given in Chan et al. (2010). A modeling approach rather similar to the one taken here is presented in He and Hodgson (2002) while a more detailed model is found in Syed et al. (2006).

Efforts specifically targeted at model development for batteries are Johnson (2002), Tremblay et al. (2007), Szumanowaski and Chang (2008). Most of those works use experimental data and try to fit a model through their data, sometimes using physically inspired basis functions. The temperature influence for batteries is discussed in Pesaran (2002). For super capacitors, a modeling approach is presented in Buller et al. (2002).

The inverter, the power electronics needed to couple battery pack and electric machine, is analyzed in Mapelli et al. (2010), while the electric machine losses are analyzed in Williamson et al. (2007).

One of the well known tools for modeling (hybrid) drivetrains is the simulation package “ADVISOR”, see Markel et al. (2002), which mainly focused on reliable prediction of behavior using simulation, for which it has been used frequently, see,

e.g., Johnson et al. (2000), Gao et al. (2007). However, there is no emphasis on simplified analytical models for online control purposes. Alternative tools are described in Butler et al. (1999), Lin et al. (2001), Onoda and Emadi (2004). Specialized approaches, like gyrator theory, are used in Routex et al. (2000).

Models are also introduced when a specific control strategy for hybrid systems is discussed. Examples are in Kao and Moskwa (1995), Shimizu et al. (1997), Tate and Boyd (2000), Lin et al. (2003), West et al. (2003), Albert et al. (2004), Sciarretta et al. (2004), Barsali et al. (2004), Lukic and Emadi (2004), Delprat et al. (2004), Tyrus et al. (2004), Plett (2004), Baisden and Emadi (2004). The paper by Tate and Boyd (2000) uses a particularly simple model.

Type-approval drive cycles are determined by regulatory bodies or by committees trying to establish the common denominator between all participants. For an example see the documents of the ECE-GRPE Working Party on Pollution and Energy (ECE/Trans/WP.29/GRPE).⁴

References

- Albert IJ, Kahrmanovic E, Emadi A (2004) Diesel sport utility vehicles with hybrid electric drive trains. *IEEE Trans Veh Technol* 53(4):1247–1256
- Bailey KE, Powell BK (1995) A hybrid electric vehicle powertrain dynamic model. In: *Proc American control conf*, Seattle, WA, USA, pp 1677–1682
- Baisden AC, Emadi A (2004) ADVISOR-based model of a battery and an ultra-capacitor energy source for hybrid electric vehicles. *IEEE Trans Veh Technol* 53(1):199–205
- Barsali S, Miulli C, Possenti A (2004) A control strategy to minimize fuel consumption of series hybrid electric vehicles. *IEEE Trans Energy Convers* 19(1):187–195
- Buller S, Karden E, Kok D, De Doncker RW (2002) Modeling the dynamic behavior of supercapacitors using impedance spectroscopy. *IEEE Trans Ind Appl* 38(6):1622–1626
- Butler KL, Ehsani M, Kamath P (1999) A Matlab-based modeling and simulation package for electric and hybrid electric vehicle design. *IEEE Trans Veh Technol* 48(6):1770–1778
- CFR40-19 (2012a) Code of federal regulations title 40—protection of environment. <http://www.gpo.gov/fdsys/pkg/CFR-2012-title40-vol19/pdf/CFR-2012-title40-vol19.pdf>
- CFR40-20 (2012b) Code of federal regulations title 40—protection of environment. <http://www.gpo.gov/fdsys/pkg/CFR-2012-title40-vol20/pdf/CFR-2012-title40-vol20.pdf>
- Chan CC, Bouscayrol A, Chen K (2010) Electric, hybrid, and fuel-cell vehicles: architecture and modelling. *IEEE Trans Veh Technol* 59(2):589–598
- Delprat S, Lauber J, Guerra TM, Rimaux J (2004) Control of a parallel hybrid powertrain: optimal control. *IEEE Trans Veh Technol* 53(3):872–881
- EEC (1970) Council directive of 20 March 1970 on the approximation of the laws of the member states on measures to be taken against air pollution by emissions from motor vehicles (70/220/EEC) plus amendments. Consolidated text of Jan 1, 2007. <http://eur-lex.europa.eu/LexUriServ/LexUriServ.do?uri=CONSLEG:1970L0220:20070101:EN:PDF>
- EEC (1980) Council directive of 16 December 1980 relating to the carbon dioxide emissions and the fuel consumption of motor vehicles (80/1268/EEC) plus amendments. Consolidated text of Feb 19, 2004. <http://eur-lex.europa.eu/LexUriServ/LexUriServ.do?uri=CONSLEG:1980L1268:20040219:EN:PDF>

⁴See http://unece.org/trans/main/wp29/wgs/wp29grpe/grpedoc_2013.html.

- Ehsani M, Gao Y, Emadi A (2010) Modern electric, hybrid electric, and fuel cell vehicles: fundamentals, theory and design, 2nd edn. CRC Press, Boca Raton
- Gao DW, Mi C, Emadi A (2007) Modeling and simulation of electric and hybrid vehicles. *Proc IEEE* 95(4):729–745
- German JM (2011) Hybrid-powered vehicles, 2nd edn. SAE, Warrendale
- Guzzella L, Sciarretta A (2005) Vehicle propulsion systems. Springer, Berlin
- He X, Hodgson JW (2002) Modeling and simulation for hybrid electric vehicles—part I. *IEEE Trans Intell Transp Syst* 3(4):235–243
- Husain I (2011) Electric and hybrid vehicles: design fundamentals, 2nd edn. CRC Press, Boca Raton
- Johnson VH (2002) Battery performance models in ADVISOR. *J Power Sources* 110:321–329
- Johnson VH, Wipke KB, Rausen DJ (2000) HEV control strategy for real-time optimization of fuel economy and emissions. In: 2000 future car congress proc, Arlington, VA. SAE paper 2000-01-1543
- Kao M, Moskwa JJ (1995) Turbocharged diesel engine modeling for nonlinear engine control and state estimation. *J Dyn Syst Meas Control* 117(1):20–30
- Lin CC, Filipi Z, Wang Y, Louca L, Peng H, Assanis D, Stein J (2001) Integrated, feed-forward hybrid electric vehicle simulation in SIMULINK and its use for power management studies. In: Advanced hybrid vehicle powertrains (SP-1607), Detroit, MI. SAE paper 2001-01-1334
- Lin CC, Peng H, Grizzle JW, Kang JM (2003) Power management strategy for a parallel hybrid electric truck. *IEEE Trans Control Syst Technol* 11(6):839–849
- Lukic SM, Emadi A (2004) Effects of drivetrain hybridization on fuel economy and dynamic performance of parallel hybrid electric vehicles. *IEEE Trans Veh Technol* 53(2):385–389
- Mapelli FL, Tarsitano D, Mauri M (2010) Plug-in hybrid electric vehicle: modeling, prototype realization, and inverter losses reduction analysis. *IEEE Trans Intell Transp Syst* 57(2):598–607
- Markel T, Brooker A, Hendricks T, Johnson V, Kelly K, Kramer B, O’Keefe M, Sprick S, Wipke K (2002) ADVISOR: a systems analysis tool for advanced vehicle modeling. *J Power Sources* 110:255–266
- Miller JM (2004) Propulsion systems for hybrid vehicles. IEE power & energy series, vol 45. IEE, London
- Onoda S, Emadi A (2004) PSIM-based modeling of automotive power systems: conventional, electric, and hybrid electric vehicles. *IEEE Trans Veh Technol* 53(2):390–400
- Pesaran AA (2002) Battery thermal models for hybrid vehicle simulations. *J Power Sources* 110:377–382
- Pistoia G (ed) (2010) Electric and hybrid vehicles: power sources, models, infrastructure and the market. Elsevier, Amsterdam
- Plett GL (2004) High-performance battery-pack power estimation using a dynamic cell model. *IEEE Trans Veh Technol* 53(5):1586–1593
- Pop V, Bergveld HJ, Danilov D, Regtien PPL, Notten PHL (2008) Battery management systems. Philips research book series, vol 9. Springer, New York
- Routex JY, Gay-Desharnais S, Ehsani M (2000) Modeling of hybrid electric vehicles using gyrator theory: application to design. In: *Proc IEEE veh technol conf*, vol 5. IEEE, New York, pp 2090–2094
- Sciarretta A, Back M, Guzzella L (2004) Optimal control of parallel hybrid electric vehicles. *IEEE Trans Control Syst Technol* 12(3):352–363
- Shimizu H, Harada J, Bland C, Kawakami K, Chan L (1997) Advanced concepts in electric vehicle design. *IEEE Trans Ind Electron* 44(1):14–18
- Syed FU, Kuang ML, Czubay J, Ying H (2006) Derivation and experimental validation of a power-split hybrid electric vehicle model. *IEEE Trans Veh Technol* 55(6):1731–1747
- Szumanowski A, Chang Y (2008) Battery management system based on battery nonlinear dynamics modeling. *IEEE Trans Veh Technol* 57(3):1425–1432
- Tate ED, Boyd SP (2000) Finding ultimate limits of performance for hybrid electric vehicles. In: Hybrid electric vehicles (SP-1560), Costa Mesa, CA. SAE paper 2000-01-3099

- Tremblay O, Dessaint LA, Dekkiche AI (2007) A generic battery model for the dynamic simulation of hybrid electric vehicles. In: Proc IEEE veh power and propul conf. IEEE, New York, pp 284–289
- Tyrus JM, Long RM, Kramskaya M, Fertman Y, Emadi A (2004) Hybrid electric sport utility vehicles. IEEE Trans Veh Technol 53(5):1607–1622
- UN/ECE (2010) Regulation No 49 of the economic commission for Europe of the United Nations (UN/ECE)—uniform provisions concerning the measures to be taken against the emission of gaseous and particulate pollutants from compression-ignition engines for use in vehicles, and the emission of gaseous pollutants from positive-ignition engines fuelled with natural gas or liquefied petroleum gas for use in vehicles. <http://eur-lex.europa.eu/LexUriServ/LexUriServ.do?uri=OJ:L:2010:229:0001:0138:EN:PDF>
- UN/ECE (2012) Regulation No 83 of the Economic Commission for Europe of the United Nations (UN/ECE)—uniform provisions concerning the approval of vehicles with regard to the emission of pollutants according to engine fuel requirements. <http://eur-lex.europa.eu/LexUriServ/LexUriServ.do?uri=OJ:L:2012:042:0001:0207:EN:PDF>
- West MJ, Bingham CM, Schofield N (2003) Predictive control for energy management in all/more electric vehicles with multiple energy storage units. In: Proc IEEE internat electric machines and drives conf, vol 1. IEEE, New York, pp 222–228
- Williamson SS, Emadi A, Rajashekara K (2007) Comprehensive efficiency modeling of electric traction motor drives for hybrid electric vehicle propulsion applications. IEEE Trans Veh Technol 56(4):1561–1572

<http://www.springer.com/978-1-4471-5075-6>

Optimal Control of Hybrid Vehicles
de Jager, B.; van Keulen, T.; Kessels, J.
2013, XVIII, 142 p., Hardcover
ISBN: 978-1-4471-5075-6